



Contents lists available at ScienceDirect

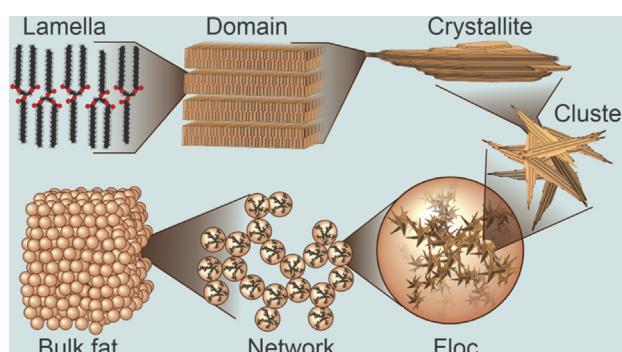
## Journal of Colloid and Interface Science

journal homepage: [www.elsevier.com/locate/jcis](http://www.elsevier.com/locate/jcis)Controlling lipid crystallization across multiple length scales by directed shear flow<sup>☆</sup>Kim Mishra<sup>a,\*</sup>, Nico Kummer<sup>a,b</sup>, Jotam Bergfreund<sup>a</sup>, Fabian Kämpf<sup>a</sup>, Pascal Bertsch<sup>a</sup>, Robin Pauer<sup>c</sup>, Gustav Nyström<sup>a,b</sup>, Peter Fischer<sup>a</sup>, Erich J. Windhab<sup>a</sup><sup>a</sup> Institute of Food, Nutrition and Health, ETH Zürich, Schmelzbergstrasse 9, 8092 Zürich, Switzerland<sup>b</sup> Laboratory for Cellulose & Wood Materials, EMPA – Swiss Federal Laboratories for Materials Science and Technology, Überlandstrasse 129, 8600 Dübendorf, Switzerland<sup>c</sup> Electron Microscopy Center, EMPA – Swiss Federal Laboratories for Materials Science and Technology, Überlandstrasse 129, 8600 Dübendorf, Switzerland

## HIGHLIGHTS

- Identification of measurable structural hierarchy levels of crystalline lipids.
- Mechanistic understanding of lipid crystallization from molecule to bulk material.
- Shear rate dependent lamellar height distribution of lipids.
- Morphology-rheology correlation using polarized light microscopy and laser diffraction spectroscopy.
- Topography of crystal clusters and crystallites using scanning electron and atomic force microscopy.

## GRAPHICAL ABSTRACT



## ARTICLE INFO

## Article history:

Received 11 August 2022

Revised 18 September 2022

Accepted 1 October 2022

Available online 6 October 2022

## Keywords:

lipid

crystallization

Shear flow

Rheology

Polarized light microscopy

## ABSTRACT

The crystallization behavior of lipids is relevant in many fields such as adipose tissue formation and regeneration, forensic investigations and food production. Using a lipid model system composed of triacylglycerols, we study the formation of crystalline structures under laminar shear flows across various length scales by polarized light-, scanning electron-, and atomic force microscopy, as well as laser diffraction spectroscopy. The shear rate during crystallization  $\dot{\gamma}_{cryst}$  influences the acyl-chain length structure and promotes domain growth into the flow direction thereby transforming the crystallites from oblate into prolate particles. Concentration dependent aggregation of crystallites into clusters is the rate limiting step for floc and floc network formation. At high  $\dot{\gamma}_{cryst}$ , fast crystallite cluster formation at smaller equilibrium diameters is promoted. The high crystallite cluster concentration induces their aggregation into flocs which form weak networks. At low  $\dot{\gamma}_{cryst}$ , floc generation is limited by the low amount of crystallite clusters leading to slow growth of larger flocs and forming of strong networks. The findings in this work

<sup>☆</sup> This document is the results of the Bridge project 20B2-1-180971/1 funded by the Swiss National Science Foundation and Innosuisse.

\* Corresponding author.

E-mail address: [mishrankar@gmail.com](mailto:mishrankar@gmail.com) (K. Mishra).

Laser diffraction spectroscopy  
Scanning electron microscopy  
Atomic force microscopy  
Lamellar stacking  
Triacylglycerol  
Tripalmitin  
 $\beta$ -polymorphic crystal  
Tilt angle  
Aggregation

have potential implications ranging from the design of injectable soft tissue fillers for adipose tissue regeneration, to the crystalline network formation in microorganism derived lipids, up to a more energy-efficient production of chocolate confectionery.

© 2022 The Authors. Published by Elsevier Inc. This is an open access article under the CC BY license (<http://creativecommons.org/licenses/by/4.0/>).

## 1. Introduction

Crystalline triacylglycerols (TAGs) belong to the lipid substance group and are omnipresent in nature playing an important role in the stabilization of multiphase systems such as emulsions [50,15] and foams [35,34,36,38] the energy storage of mammals [39], plants [26] and microorganisms [14], the surgical removal of adipose tissue [51], injectable soft tissue fillers for adipose tissue regeneration [8], forensic investigations [55], and drug delivery systems [5]. TAGs with high content of saturated fatty acids (SFAs), commonly named fats, are used in packaged and fast foods, personal care as well as cosmetic products due to their high functionality originating from the crystalline phase [16,54,58,42,30]. In case of African oil palm (*Elaeis guineensis* Jacq.) derived TAGs, the low apparent production cost and hence high demand has led to severe deforestation in tropical regions [58,7]. Furthermore, the intake of TAGs with high amount of SFAs has been associated with cardiovascular diseases in humans [42,30,16,54]. Consequently, recent studies focused on replacing TAGs with high SFA content with other lipids [42,30,16,54]. However, the replacements usually lead to different organoleptic experiences leading to low consumer acceptance [25]. Therefore, for future replacement strategies it is of great importance to understand the crystal structure of TAGs with SFAs. The crystalline structure of TAGs has been investigated intensively by X-ray diffraction (XRD) revealing the short- and long spacing of the TAG alkyl-chains [10,27,24], which are characteristic for specific polymorphic forms [52,53]. Several studies have correlated the polymorphic form of TAGs with their macroscopic bulk properties such as their viscosity, shear and elastic modulus [37,3,11,40], the spreadability of margarine [53], and in case of cocoa butter even with the snap, gloss and organoleptic properties of chocolate [9,56,12,25]. For tripalmitin (TP), the characteristic short spacing values of the  $\beta$ -polymorphic form ( $\beta$ -TP) are 0.37, 0.385, and 0.46 nm [21,22,19,27]. The long spacing of  $\beta$ -TP, which mirrors the distance between methyl end groups of the alkyl-chains [31,22], originates from a double chain length (DCL) structure [28] as depicted in Figure S1. Reported  $\beta$ -TP long spacings range from 3.2 to 4.8 nm, which has led to much controversy regarding the existence of  $\beta$  sub-modifications [21,22,19,13,10,27]. The different  $\beta$  sub-modifications are characterized by their tilt angle  $\tau$  as shown in Figure S1. Reported values for the  $\beta$ -TP tilt angle vary from 44 to 75° [62,19,13,31]. The tilt angle  $\tau$  can be calculated for triclinic DCL  $\beta$ -triacylglycerols: [19]:

$$\tau = \arcsin \frac{3d_{001}}{(n + n_0)c_s} \quad (1)$$

where  $d_{001}$  is the  $\beta$  long spacing,  $n_0$  a constant of 6.62,  $n$  the total number of C-atoms in the acyl-chains and  $c_s$  the subcell period along the acyl-chain of 0.2545 nm equal to the distance between 3 C-atoms in the alkyl-chain [47]. Calculating the tilt angle for  $\beta$ -TP with  $d_{001} = 4.03\text{--}4.07$  nm [22] and  $n = 48$ , we get  $\tau = 60\text{--}61^\circ$ . Another calculation method was proposed in Marangoni & Wesdorp [31, Chapter 1]:

$$\tau = 90 - \arccos \frac{d_{001}(\beta)}{d_{001}(\alpha)} \quad (2)$$

where  $d_{001}(\beta) = 4.06$  nm [10],  $d_{001}(\alpha) = 4.56$  nm [10] leading to 62.9°. Zdravkova & Van der Eerden [62] measured the thickness of a  $\beta$ -TP monolayer by AFM to be  $3.3 \pm 0.1$  nm, resulting in  $\tau = 43.8\text{--}47.3^\circ$ .

Despite the vast literature on TAG crystal polymorphic form, nano- and microstructure, relatively little studies investigated the morphology of the formed crystalline structures across multiple length scales from single lamellae to aggregated flocs [32,47,49,1,2,17,46,44]. No standard procedure exists to characterize the morphology of crystalline TAGs across different length scales. Consequently, this study investigated the crystallization of tripalmitin (TP) in medium-chain triacylglycerol (MCT) oil under defined shear- and supercooling rates in a Couette geometry. The TP-MCT oil system was previously shown to be monotectic under rapid formation of  $\beta$ -polymorphic TP crystals and was therefore suited as a model system for TAG crystallization [34]. Rotational shear rheometry enabled the TP-MCT melt crystallization at defined shear rates. Polarized light microscopy (PLM), laser diffraction spectroscopy (LDS), scanning electron microscopy (SEM), X-ray diffraction (XRD), and atomic force microscopy (AFM) were applied to investigate the size and morphology of the formed crystalline structures at different length scales as illustrated in Fig. 1. The nomenclature of the hierarchical structure proposed in Fig. 1 was adapted from previous studies [57,1,2,29,30]. The spacing between the alkyl-chains of the crystalline TAG molecules (short spacing) is accessible by XRD. The acyl-chain length structure is accessible by AFM and XRD, where XRD measures the projection of the acyl-chain (long spacing) and AFM the actual lamellar thickness. AFM determines domain dimensions composing a crystallite. The domain is also referred to as "nano-platelet" or "primary crystal" and domain height was previously calculated using the Scherrer equation [2,1]. The 3D crystallite morphology is determined by AFM, whereas the 2D crystallite dimensions are imaged by SEM. On the crystallite cluster level, SEM gives detailed morphological as well as qualitative size information. LDS measures statistically relevant size information and PLM gives a qualitative estimation of crystallite cluster size which is essential to classify the LDS results. Floc morphology and qualitative size are assessed by PLM, whereas quantitative size information is acquired by LDS. The aggregation of flocs into a network can be qualitatively assessed by PLM and quantitatively by rheological measurements. This holistic approach allows to identify suitable methods for each TAG structural hierarchy level and offers new insights on the effect of shear flows on TAG crystal formation.

## 2. Materials and Methods

**MCT oil purification:** Purification of a medium-chain triglyceride (MCT) oil (C10:C8 = 30:70, BASF, Myritol 318) was performed with the Florisil® adsorbents (MgO·SiO<sub>2</sub>, 100–200 mesh, Sigma Aldrich) to remove polar contaminants such as mono- and diacylglycerols as well as free fatty acids as described by Bergfreund et al. [4]. 40 g of Florisil® adsorbents were mixed with 1000 g of MCT oil and gently stirred overnight. The MCT oil was then fil-

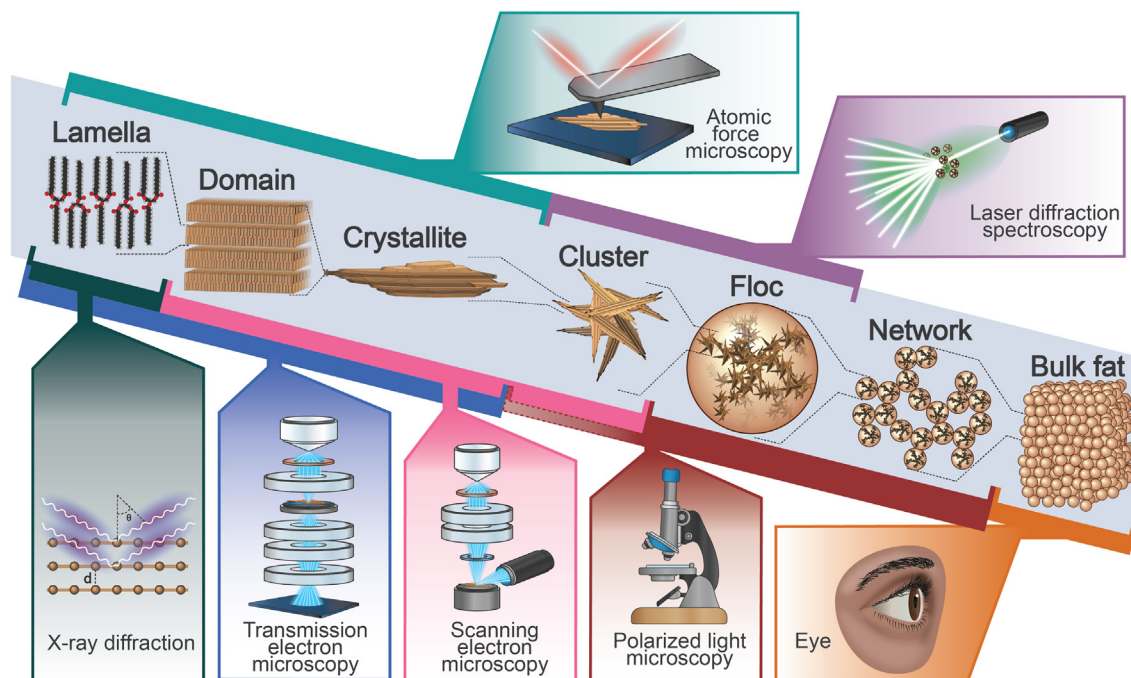


**Fig. 1.** Measurement method allocation with the hierarchical structure of crystalline TAGs. XRD, AFM, and TEM [1,2] measure the long spacing or lamellar thickness. AFM measures the domain dimensions in 3D. AFM and SEM measure the crystallite dimension in 3- and 2 D, respectively. SEM, LDS, and PLM visualize individual crystallite clusters. LDS and PLM yield quantitative or qualitative information on floc size. PLM gives qualitative insight into the aggregation of flocs into a network. The bulk crystalline TAG (fat) is visible by the naked eye. The nomenclature of the hierarchical structure was adapted from previous studies [1,2,29,30,57].

tered and centrifuged at 15000 g before carefully harvesting the supernatant.

**Dissolution into purified MCT oil:** 1 mol% glycerol tripalmitate (tripalmitin, TP) (807.3 g/mol, purity  $\geq 98.5$ , Acros Organics) was dissolved into purified MCT oil (C10:C8 = 30:70, BASF, Myritol 318) at 90 °C and gently stirred for 10 min to create a TP-MCT melt.

**Crystallization and rheometry:** A shear rheometer (MCR 302, Anton Paar, Graz, Austria) equipped with a CC27 Couette system was used. The Couette was pretempered to 60 °C before the TP-MCT melt was poured at 90 °C into the gap between rotor and stator. The TP-MCT melt was equilibrated 10 min at 60 °C applying the same shear rate as used for the subsequent isothermal crystallization step. After the equilibration step, a cooling step was applied to reach 20 °C at 5 °C/min. Once the 20 °C were reached, an isothermal crystallization step was performed for 60 min to create a TP-MCT crystal-melt suspension (CMS). The crystallization shear rates  $\dot{\gamma}_{cryst}$  applied were  $10^0$ ,  $10^1$ ,  $10^2$ , and  $10^3$  s $^{-1}$ . After the isothermal crystallization step was complete, a shear rate ramp from 0.3 to 1000 s $^{-1}$  was conducted with 5 steps per decade and a measurement time of 2 s per step.

**Laser diffraction spectroscopy:** The LS13 320 laser diffraction particle size analyzer (Beckman Coulter, Brea CA, USA) with a universal liquid module was applied. As a continuous phase Hydriol® SOD.24 (Hydriol AG, Wettingen, Switzerland) was used. The TP-MCT CMS was introduced into the liquid module directly after the isothermal crystallization step and pumped in a loop through the scattering chamber. The pump speed of the LDS device was set to 60% and the diffraction pattern was measured during 90 s. The diffraction pattern was interpreted using the Fraunhofer model. Polarization intensity differential scattering (PIDS) data was included. At least 3 true replicates were performed and averaged.

**Light microscopy:** Polarized light microscopy (PLM) (Leica DM6, Leica Microsystems AG, Heerbrugg, Switzerland) was used. A TP-MCT CMS drop was poured directly after the isothermal crystallization step on a microscopy slide, covered with a cover glass

and analyzed. Sonicated samples were tip sonicated in the Couette cell at 200 W and 24 kHz during 10 s with a Hielscher UP200S (Teltow, Germany) before being dropped on the microscopy slide. The microscopy room was temperature controlled to 20 °C.

**Crystal harvesting:** After the isothermal crystallization step, the TP-MCT CMS was poured on a vacuum filter with a 1  $\mu$ m retention glassfibre filter (693, VWR international GmbH, Dietikon, Switzerland) connected to a 200 mbar vacuum pump. The resulting filter cake was harvested and rinsed with 20 °C ethanol before being filtered a second time with the same filter type. The filter-cake was harvested dried for 3 h at 20 °C and 200 mbar to remove excess solvent.

**Atomic force microscopy:** The harvested crystals (15 mg) were mixed with 5 ml ethanol that was pre-cooled to –20 °C in the freezer. The dispersions were tip sonicated to break up crystallite clusters and promptly dropped (100  $\mu$ l) onto freshly cleaved, unmodified mica. The excess liquid was immediately blown away with pressurized air without a rinsing step to prevent dissolution of the tripalmitin crystallites. The imaging was performed on a Bruker Icon 3 AFM in tapping mode at a scan rate of 0.4 Hz and at a resolution of 1024x1024 lines. The raw images were flattened and analyzed with the Bruker Nanoscope software. The thickness of the lamellae was measured by fitting the following asymptotic equation on each z-step:

$$z(x, y) = A_1 + \frac{(A_2 - A_1)}{1 + 10^{(\log[xy_0] - xy)p}} \quad (3)$$

where  $z$  denotes the position along the  $z$ -axis,  $xy$  the position in the  $xy$ -plane,  $A_1$  the bottom and  $A_2$  the top asymptote,  $p$  the slope of the curve, and  $\log[xy_0]$  the center of the step. The lamellar thickness was then calculated as  $A_2 - A_1$ . OriginPro 2021 (OriginLab Corporation, Northampton, USA) was used for the fitting.

**Scanning electron microscopy:** As described above the harvested crystals were mixed with –20 °C ethanol at a concentration of 3 mg/ml. Subsequently, the suspensions were either vortexed for 30 s to examine crystallite clusters or tip sonicated according



to the AFM protocol to break up crystallite clusters and resolve the single crystallite morphology. A  $10^2$  ml droplet of the suspensions was deposited on freshly cleaved mica as already done for the AFM sample preparation. The mica was then carbon coated with pulse vaporization by means of carbon filament (CCU-010, Safematic GmbH, Zizers, Switzerland). A vacuum below  $10^{-5}$  mbar was applied to deposit carbon films with a layer thickness per pulse of about 0.9 nm amounting to a total layer thickness of 5 nm. The carbon coated micas were then transferred to the SEM (ESEM Quanta FEG650, Thermo Fisher, Waltham, USA) onto a cooled Peltier stage at  $1^\circ\text{C}$ . A vacuum of 0.6 mbar was applied. A field emitter (Schottky-emitter) with an electron acceleration voltage of 5 kV was used at a distance of 9–11 mm of the sample surface. A large field detector and concentric backscatter detector were used to capture secondary as well as reflected electrons.

**Differential scanning calorimetry:** A differential scanning calorimeter (DSC 3+, Mettler Toledo GmbH, Greifensee, Switzerland) was used to investigate the melting behavior of the harvested TP crystals. For each sample, triplicates were measured. Sample weight was  $5 \pm 0.2$  mg for every triplicate. Samples were weighted into 40  $\mu\text{l}$  aluminium crucibles (Mettler Toledo GmbH, Greifensee, Switzerland) that weighed  $50.49 \pm 0.2$  mg. Heat flow at a given temperature was evaluated using the STARE-Software (SW 8.1, Mettler Toledo GmbH, Greifensee, Switzerland). Peak positions were identified using the peak finder function of the OriginPro 2021 software (OriginLab Corporation, Northampton, USA).

**X-ray diffraction:** An X-ray diffractometer (D8 advanced, Bruker GmbH, Karlsruhe, Germany) was used to characterize the samples in this study. The diffractometer radiation source was Cu-K $\alpha$ 1 with a wavelength of  $\lambda = 0.15406$  nm and  $E_{\text{beam}} = 40$  keV. Samples were rotated but not tempered during analysis. A step size of  $0.02^\circ$  was chosen for the scans between  $2\theta = 5$  and  $40^\circ$ . Duplicates were measured. For the scans between  $2\theta = 1$  and  $7^\circ$ , a step size of  $0.00395^\circ$  was chosen. Quadruplicates were measured. Peaks were analyzed using the OriginPro 2021 software (OriginLab Corporation, Northampton, USA). Firstly, the baseline of the peaks was calculated by asymmetric least square smoothing and then subtracted. Then the peak positions were identified using the peak finder function. The full width at half maximum (FWHM) was calculated using a Gaussian fit.

**Statistical analysis:** The y-error bars depicted in Fig. 4 are calculated standard deviations  $s$  of the sample using the following equation:

$$s = \sqrt{\frac{1}{N} \sum_{i=1}^N (x_i - \bar{x})^2} \quad (4)$$

where  $\bar{x}$  is the mean of the entire sample population, and  $N$  the number of replicates.

The z-steps presented in Fig. 6(F) and 7(F) were determined using non-linear curve fitting. The orthogonal distance regression iteration algorithm without weights was used. The adjusted  $R^2$  was  $> 0.99$  for all fits. The fitting parameters  $A_1, A_2, p$ , and  $\log[xy_0]$  were tested with a two-tailed t-test. For  $A_1, A_2$ , and  $\log[xy_0]$ ,  $\text{Prob} > |t|$  was rejected at  $\alpha = 0.05$ . For  $p$ ,  $\text{Prob} > |t|$  could not be rejected at  $\alpha = 0.05$  in 8 (Fig. 6(F)) and 13 (7(F)) cases.

### 3. Data availability

The data presented in this article is available at <https://doi.org/10.3929/ethz-b-000523967> or <https://www.research-collection.ethz.ch/handle/20.500.11850/523967>. The profiles used to identify the z-steps for the histograms presented in Fig. 6(F) and 7(F) are available via the same link.

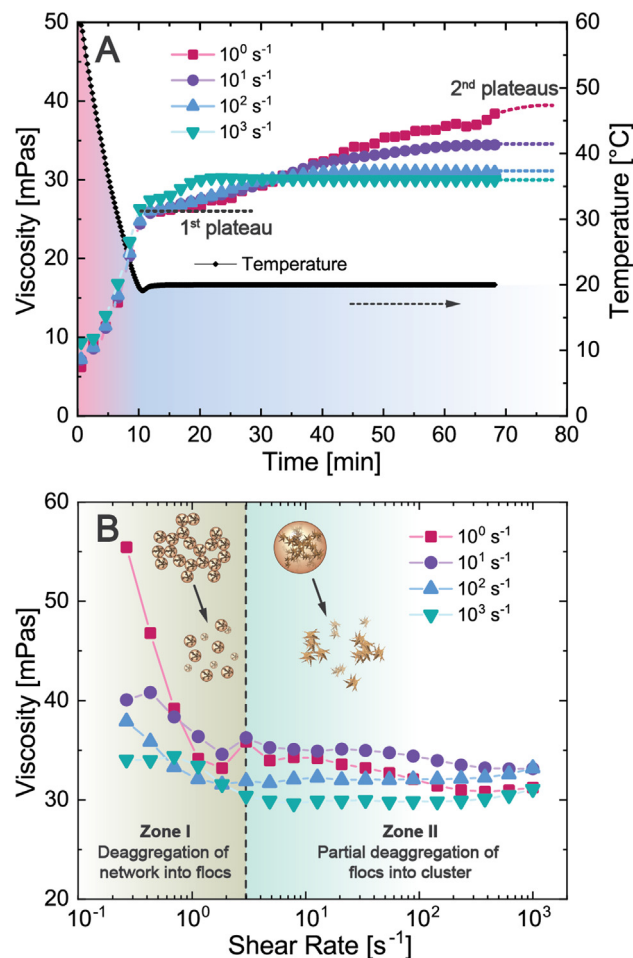


**Fig. 2.** (A) The viscosity and temperature as function of time for 1 mol% TP in MCT during crystallization at  $\dot{\gamma}_{\text{cryst}} = 10^0, 10^1, 10^2$ , and  $10^3 \text{ s}^{-1}$ . Every curve represents the mean value of 9 replicates. Raw data was reduced by averaging 5 adjacent data points. (B) The viscosity as function of shear rate for 1 mol% TP in MCT directly after isothermal crystallization in (A) had been completed. Every curve represents the mean value of 3 replicates.

### 4. Results

The TP-MCT system was crystallized by dissolving 1 mol% TP in purified MCT oil at  $90^\circ\text{C}$  resulting in a TP-MCT melt. The melt was transferred into a rheometer equipped with a Couette geometry at  $60^\circ\text{C}$ . The TP-MCT melt was cooled to  $20^\circ\text{C}$ , corresponding to a supercooling temperature  $\Delta T = 10^\circ\text{C}$  [34], at  $5^\circ\text{C}/\text{min}$  applying crystallization shear rates  $\dot{\gamma}_{\text{cryst}}$  of  $10^0, 10^1, 10^2$  and  $10^3 \text{ s}^{-1}$  thereby forming a TP-MCT crystal-melt suspension (CMS). During the cooling and subsequent isothermal holding step, the viscosity at the set  $\dot{\gamma}_{\text{cryst}}$  was recorded. The results are displayed in Fig. 2(A). During the cooling step, no difference between the varying  $\dot{\gamma}_{\text{cryst}}$  is apparent due to the Newtonian flow behavior of the pure melt. Reaching the isothermal holding step, the curves start to diverge depending on the applied  $\dot{\gamma}_{\text{cryst}}$  indicating the formation of a crystal network. All curves reach a first plateau after the cooling step is completed, followed by a second plateau during the isothermal crystallization. The transition time from the first to the second plateau as well as the plateau height is decreased with increasing  $\dot{\gamma}_{\text{cryst}}$ . The decreased transition time from first to second plateau indicates the accelerated formation of a crystalline network and its stable spatial arrangement. The decreased plateau heights indicate non-Newtonian flow behavior. To compare the rheology of the generated TP-MCT CMSs, a shear rate ramp was conducted directly after

the isothermal crystallization step. Fig. 2(B) shows the viscosity of the produced TP-MCT CMSs as function of the shear rate  $\dot{\gamma}$ . For all TP-MCT CMSs an initial strong decrease of the viscosity between  $\dot{\gamma} = 0.1$  and  $3 \text{ s}^{-1}$  (Zone I) is apparent. For TP-MCT CMSs produced at  $\dot{\gamma}_{\text{cryst}} = 10^0$  and  $10^1 \text{ s}^{-1}$ , a weak viscosity decrease between  $\dot{\gamma} = 3$  and  $1000 \text{ s}^{-1}$  (Zone II) follows the initial strong decrease. The initial viscosity decrease depends strongly on the shear rate applied during crystallization  $\dot{\gamma}_{\text{cryst}}$ . With increasing  $\dot{\gamma}_{\text{cryst}}$ , the viscosity decrease in Zone I is less pronounced due to the reduced network formation of the crystalline structures during the isothermal crystallization period. The weak viscosity decrease in Zone II is related to a further deaggregation process of the network forming crystalline structures into smaller units leading to the release of entrapped liquid continuous phase, which reduces the effective crystal volume fraction  $\Phi_{\text{SFC}}^{\text{eff}}$  and consequently leads to a drop in viscosity [61]. The reduction of  $\Phi_{\text{SFC}}^{\text{eff}}$  as function of the applied  $\dot{\gamma}$  has been described previously [61,48,60,59]. To allocate the formed crystalline structures to the nomenclature proposed by Tang & Marangoni [57] as illustrated in Fig. 1, polarized light microscopy (PLM) was performed.

Fig. 3(A–D) show PLM images of TP-MCT CMSs taken directly after the isothermal crystallization at different  $\dot{\gamma}_{\text{cryst}}$  was completed. Additional images are displayed in Figure S2. For  $\dot{\gamma}_{\text{cryst}} = 10^0$  and  $10^1 \text{ s}^{-1}$ , large brush-like flocs aggregate into networks. Increasing  $\dot{\gamma}_{\text{cryst}}$  to  $10^2 \text{ s}^{-1}$ , large brush-like flocs as well as smaller spherical flocs are visible. The large flocs disappear for highest  $\dot{\gamma}_{\text{cryst}} = 10^3 \text{ s}^{-1}$ , where exclusively small spherical flocs are apparent. To visualize the single clusters and flocs, the TP-MCT CMSs were tip sonicated during 10 s. Fig. 3(E–H) shows the same samples as displayed in Fig. 3(A–D) after tip sonication. For  $\dot{\gamma}_{\text{cryst}} = 10^0$ ,  $10^1$ , and  $10^2 \text{ s}^{-1}$  the sonication step has not only deaggregated the flocs but also partially disrupted the crystallite cluster aggregates within the flocs. Consequently, loosely packed flocs with similar size and packing density are apparent. Highest  $\dot{\gamma}_{\text{cryst}}$  of  $10^3 \text{ s}^{-1}$  produced significantly smaller single flocs as well as single crystallite clusters. The images presented in Fig. 3(A–H) confirm the rheological findings: The main viscosity drop in Zone I is related to the disruption of the floc-floc bridges between the brush-like flocs, which are responsible for network formation. With increasing  $\dot{\gamma}_{\text{cryst}}$ , less floc-floc bridges are present after isothermal crystallization and hence the initial viscosity drop is less pronounced. The viscosity

drop in Zone II is due to the partial disruption of the flocs into crystallite clusters thereby releasing liquid continuous phase and reducing  $\Phi_{\text{eff}}$ . For TP-MCT CMSs produced at  $\dot{\gamma}_{\text{cryst}} = 10^2$  and  $10^3 \text{ s}^{-1}$ , the absence of the viscosity drop in Zone II is due to smaller spherical flocs, which are more resistant to deaggregation under shear flows. To obtain quantitative data on floc size and increase the spatial resolution to measure crystal cluster size, laser diffraction spectroscopy (LDS) was performed.

Fig. 4(A) shows the representative diameter  $x_{90,3}$  of the floc and cluster size of the TP-MCT CMSs as function of the crystallization shear rate  $\dot{\gamma}_{\text{cryst}}$  with and without tip sonication prior to analysis. For TP-MCT CMSs without sonication, the LDS data confirms the findings from the PLM images both qualitatively as well as quantitatively. Up to  $\dot{\gamma}_{\text{cryst}}$  of  $10^2 \text{ s}^{-1}$ , the diameter of the diffracting crystalline structure remains almost constant between 150 and 175  $\mu\text{m}$  before dropping to 60  $\mu\text{m}$  at  $\dot{\gamma}_{\text{cryst}} = 10^3 \text{ s}^{-1}$ . Judging from the PLM images, this size corresponds to one brush-like or spherical floc indicating that the flow regime in the LDS channel exceeds the required shear rate of  $3 \text{ s}^{-1}$  to break up floc-floc bridges. Taking into account the size density distributions as shown in Fig. 4(A) and Figure S3, the strong drop of  $x_{90,3}$  at  $\dot{\gamma}_{\text{cryst}} = 10^3 \text{ s}^{-1}$  is due to an increasingly multimodal distribution indicating that apart from flocs, also crystal clusters are present. To exclude that the drop in  $x_{90,3}$  at  $\dot{\gamma}_{\text{cryst}} = 10^3 \text{ s}^{-1}$  is related to polymorphic changes, XRD and DSC measurements were conducted as shown in Figure S4. Regardless of the applied  $\dot{\gamma}_{\text{cryst}}$ , the  $\beta$ -polymorphic form is present. TP-MCT CMSs measured after tip sonication show lower  $x_{90,3}$  for all investigated  $\dot{\gamma}_{\text{cryst}}$  compared to the unsonicated samples. This indicates that the loose flocs present after sonication are completely deaggregated into crystallite clusters and remain deaggregated in the flow regime of the LDS measurement. A steady decrease of the crystallite cluster size from 77 to 36  $\mu\text{m}$  with increasing  $\dot{\gamma}_{\text{cryst}}$  is apparent. This gradual decrease was not expected, judging from the PLM images where the crystallite clusters of  $\dot{\gamma}_{\text{cryst}} = 10^0$ ,  $10^1$ , and  $10^2 \text{ s}^{-1}$  appear similar in size. However, the density distributions in Fig. 4(B) show that for  $\dot{\gamma}_{\text{cryst}} = 10^0 \text{ s}^{-1}$  a slightly multimodal distribution prevails originating from not completely deaggregated flocs. Regardless of the multimodality, a decrease in mean crystallite cluster size is evident judging from the shift of the main peak towards lower diameters for increasing  $\dot{\gamma}_{\text{cryst}}$ . From the findings in Fig. 4, we deduce that the acting shear stresses are gradually decreasing crystallite cluster size while decreasing the floc size in

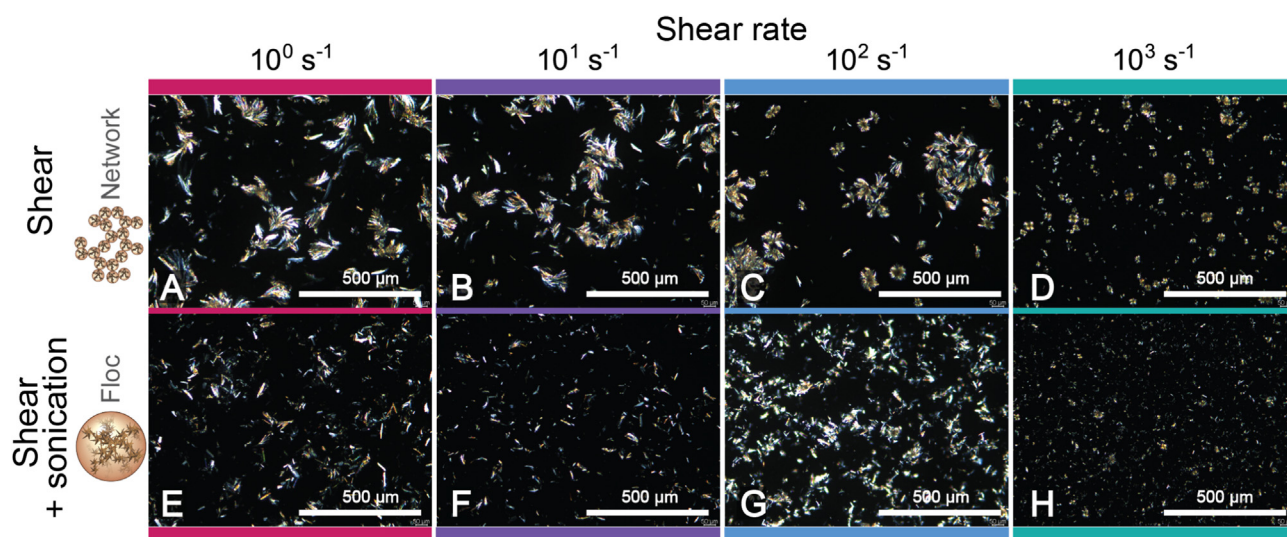
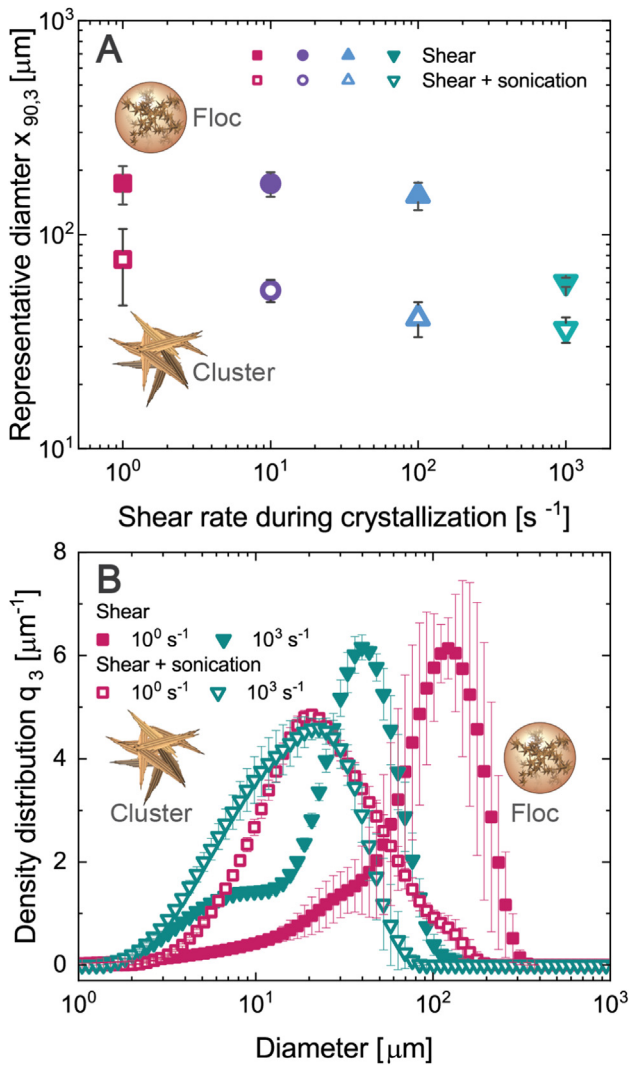


Fig. 3. TP-MCT CMS PLM images obtained after isothermal crystallization at crystallization shear rates  $\dot{\gamma}_{\text{cryst}}$  of  $10^0$ ,  $10^1$ ,  $10^2$ , and  $10^3 \text{ s}^{-1}$ . Samples were either directly imaged after crystallization (A–D) or additionally tip sonicated before imaging (E–H).



**Fig. 4.** (A) The volume weighted 90<sup>th</sup> percentile diameter  $x_{90,3}$  of TP-MCT CMSs after isothermal crystallization at crystallization shear rates  $\dot{\gamma}_{cryst}$  of  $10^0$ ,  $10^1$ ,  $10^2$  and  $10^3$   $s^{-1}$  measured by LDS. Samples were either directly measured after crystallization or additionally tip sonicated. (B) The LDS density distribution  $q_3$  of TP-MCT CMS crystallized at  $\dot{\gamma}_{cryst} = 10^0$ , and  $10^3$   $s^{-1}$ . Samples were either directly measured after crystallization or additionally tip sonicated. The curves in (A) and (B) represent the mean value of 3 replicates and the indicated error bars were calculated according to Eq. 4.

a threshold-like manner. This can be explained by displaying the formation of crystallite clusters and flocs as coupled reactions:



where C is crystallite-, CC crystallite cluster-, and F floc concentration. Assuming that the system is not limited by nucleus formation [45] and that  $k_2 \gg k_1$ ,  $k_1 > k_{-1}$ , and  $k_2 > k_{-2}$  and that the activation energy  $E_a$  is smaller than the thermal energy  $k_B T$  for both reactions, the rate determining reaction rate will be  $k_1$  which describes the aggregation of the crystallites into crystallite clusters. From Eq. 5, we deduce that for  $\dot{\gamma}_{cryst} = 10^0$  and  $10^1$   $s^{-1}$ ,  $k_1$  is still the rate limiting step and consequently the aggregation of crystallite clusters into flocs has not reached complete equilibrium during the isothermal crystallization step. For every deaggregated floc, many more are aggregating. Hence, below  $\dot{\gamma}_{cryst} = 10^2$   $s^{-1}$  the equilibrium floc size can not be reached due to the lack of crystallite clusters. At  $\dot{\gamma}_{cryst} = 10^2$  and  $10^3$   $s^{-1}$ ,  $k_1 \approx k_2$ , which means that  $k_1$  is no longer the rate limiting step and that there is an equilibrium between crystallite

cluster and floc formation. This is in accordance with Fig. 2(A), where the second viscosity plateau for TP-CMS crystallized at  $\dot{\gamma}_{cryst} = 10^0$   $s^{-1}$  is not completely reached and for  $\dot{\gamma}_{cryst} = 10^1$   $s^{-1}$  the plateau has just been reached after the isothermal crystallization step. For  $\dot{\gamma}_{cryst} = 10^2$   $s^{-1}$ , the second plateau is reached after  $\approx 35$  min and for  $\dot{\gamma}_{cryst} = 10^3$   $s^{-1}$  after  $\approx 20$  min. Hence, for  $\dot{\gamma}_{cryst} \geq 10^2$   $s^{-1}$  the measured floc size corresponds to the equilibrium floc size at the corresponding  $\dot{\gamma}_{cryst}$ . The equilibrium crystallite cluster/floc diameter  $x_{eq}$  is calculated using the Capillary number  $Ca$ , which describes the ratio of viscous forces and the bonding forces within a particulate agglomerate [6,20]:

$$x_{eq} = \frac{Ca_c \sigma}{\eta \dot{\gamma}} \quad (6)$$

where  $Ca_c$  is the system specific critical Capillary number for crystallite cluster/floc break-up and  $\sigma$  the interfacial tension. Concluding the LDS results, the difference between the gradual decrease of crystallite cluster size compared to the abrupt decrease of floc size results from the rate limiting step of crystallite cluster formation. The increasing shear rate during crystallization  $\dot{\gamma}_{cryst}$  reduces the activation energy  $E_a$  for crystallite cluster and floc formation due to the increased likelihood of encounter. This increases crystallite cluster formation and subsequent aggregation into flocs enabling both reactions to be at equilibrium. At equilibrium, the shear stresses acting on the crystallite clusters/flocs is decreasing the equilibrium diameter according to Eq. 6. To confirm the order of magnitude of the crystallite cluster size as function of  $\dot{\gamma}_{cryst}$ , scanning electron microscopy (SEM) was performed.

Fig. 5 shows SEM images of TP-MCT CMSs crystallized at (A–B, E–F)  $\dot{\gamma}_{cryst} = 10^0$   $s^{-1}$  and (C–D, G–H)  $\dot{\gamma}_{cryst} = 10^3$   $s^{-1}$  without (A–D) and with (E–H) sonication prior to deposition on the mica. Fig. 5(A–B) show crystallite clusters crystallized at  $\dot{\gamma}_{cryst} = 10^0$   $s^{-1}$  where the longest dimension lies between 30 and 80  $\mu m$ . The clusters vary in size and number of single crystallites composing the cluster. Fig. 5(C–D) show crystallite clusters crystallized at  $\dot{\gamma}_{cryst} = 10^3$   $s^{-1}$  where the longest dimension lies between 10 and 40  $\mu m$ . Less variability in cluster size and number of single crystallites composing the cluster is apparent. Furthermore, single crystallites with high aspect ratios are visible. The SEM images confirm the findings presented in Fig. 4 regarding the impact of  $\dot{\gamma}_{cryst}$  on crystallite cluster size both qualitatively and quantitatively. Fig. 5(B) shows a large and loosely aggregated crystallite cluster resulting from the low shear stresses acting at  $\dot{\gamma}_{cryst} = 10^0$   $s^{-1}$ . Fig. 5(D) shows a small and densely packed crystallite cluster formed at the high acting shear stresses at  $\dot{\gamma}_{cryst} = 10^3$   $s^{-1}$ . From the strongly aggregated crystallite clusters, it is difficult to distinguish the single crystallites. To visualize the individual crystallites composing the clusters, a sonication step was introduced before imaging. The results are displayed in Fig. 5(E–H). At  $\dot{\gamma}_{cryst} = 10^0$   $s^{-1}$ , oblate crystallites, where the length and width have similar dimensions ranging from 3 to 15  $\mu m$  are apparent. Small discrete domains are visible on some crystallites. They vary in shape, size and position with respect to the crystallite. For  $\dot{\gamma}_{cryst} = 10^3$   $s^{-1}$ , oblate and prolate crystallites are apparent. The prolate crystallites show an aspect ratio  $> 1$ , whereas the width and length of the oblate crystallites are almost equal. The largest dimension of the crystallites ranges from 1 to 8  $\mu m$ . Fewer and less discrete small domains are visible on the crystallites compared to crystallites produced at  $\dot{\gamma}_{cryst} = 10^0$   $s^{-1}$ . The difference in size and morphology between crystallites formed at  $\dot{\gamma}_{cryst} = 10^0$  and  $10^3$   $s^{-1}$  can be explained by calculating the Peclet number ( $Pe$ ) acting on a crystallite with a given diameter  $x$  at a given shear rate  $\dot{\gamma}$  [33]:

$$Pe = \frac{\dot{\gamma}}{D_r} = \frac{\dot{\gamma} \pi \eta x^3}{3 k_B T} \quad (7)$$



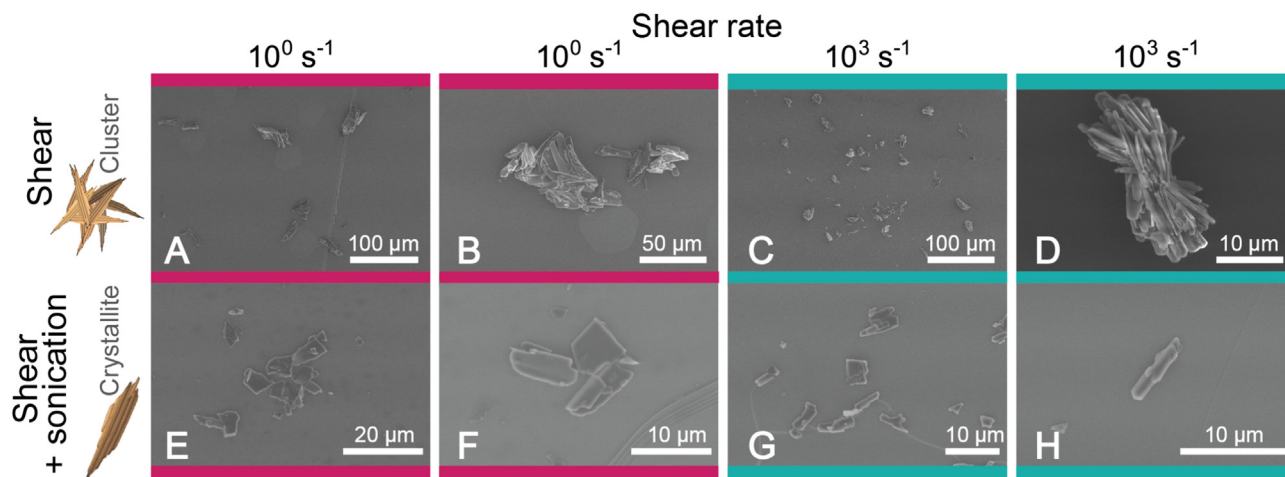


**Fig. 5.** SEM images of the harvested TP crystalline phase after isothermal crystallization. The crystalline phase was either suspended in ethanol without sonication (A–D) or suspended in ethanol and tip sonicated (E–H) prior to imaging. A, B, E, and F were crystallized at a shear rate  $\dot{\gamma}_{cryst}$  of  $10^0 \text{ s}^{-1}$  and C, D, G, and H crystallized at a shear rate  $\dot{\gamma}_{cryst}$  of  $10^3 \text{ s}^{-1}$ .

where  $D_r$  is the rotary diffusivity,  $k_B$  the Boltzmann constant,  $T$  the temperature, and  $\eta$  the viscosity of the fluid surrounding the crystallite. At  $Pe = 10$ , particle orientation can be assumed [23]. Solving Eq. 7 for  $x$  using  $Pe = 10$  and  $\dot{\gamma} = 10^0/10^3 \text{ s}^{-1}$ , we get  $x_{Pe10} = 1.0 \text{ μm}$  and  $110 \text{ nm}$ , respectively. However, during nucleation, only crystal nuclei reaching a critical diameter  $x_c$  will grow further [33]. Follow-

ing the calculations of Mazzanti et al. [33] as shown on page S6 and S7 of the supporting information, we get a critical diameter  $x_c$  of  $55 \text{ nm}$ . Combining the critical diameter for orientation  $x_{Pe10}$  and the critical diameter for nucleus growth  $x_c$ , we gather that at  $\dot{\gamma} = 10^3 \text{ s}^{-1}$  the crystallite nucleus does not experience the shear flow until at least 1 dimension reaches  $110 \text{ nm}$ . The dimension

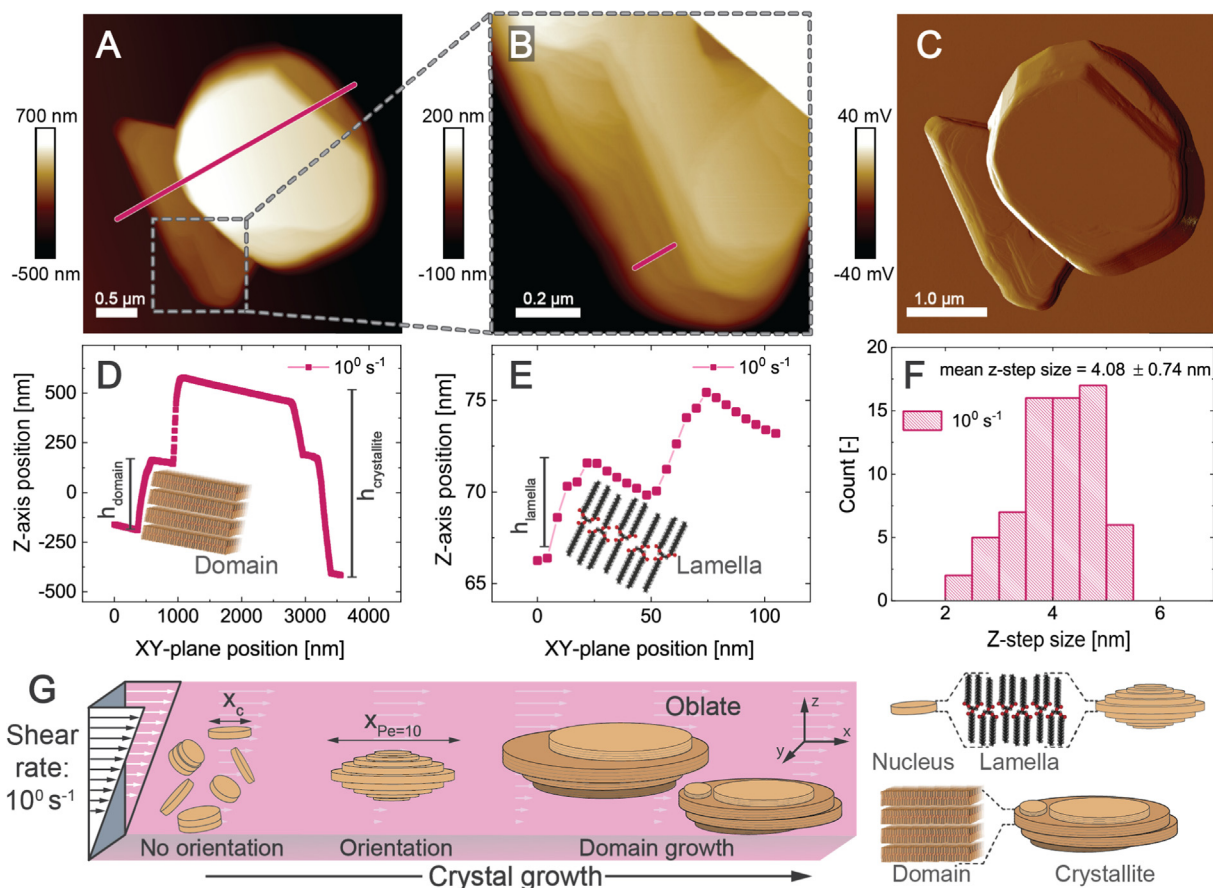


**Fig. 6.** AFM (A–B) height and (C) amplitude image of a crystallite isolated from TP-MCT CMS isothermally crystallized at  $\dot{\gamma}_{cryst} = 10^0 \text{ s}^{-1}$ . (D–E) are the z-axis readings as function of the xy-plane of the indicated red lines in (A–B), respectively. (F) shows the histogram of the z-step size indicated in (E). A total of 69 steps were evaluated with a mean step size =  $4.08 \text{ nm}$ , a minimum step size =  $2.38 \text{ nm}$ , a maximum step size =  $5.43 \text{ nm}$ , and a median step size =  $4.10 \text{ nm}$ . (G) The proposed mechanism of nucleus growth and domain propagation into a crystallite at  $\dot{\gamma}_{cryst} = 10^0 \text{ s}^{-1}$ .

exceeding 110 nm will be oriented in the shear flow field. After orientation, crystallite growth in the x-axis (direction of the flow field) leads to less drag compared to growth in the y-axis (direction of vorticity) or in the z-axis (direction of shear gradient). At  $\dot{\gamma}_{cryst} = 10^0 \text{ s}^{-1}$ , the crystallite nucleus does not experience the shear flow field until at least 1 dimension reaches 1.0  $\mu\text{m}$ . Hence, from the generation of the nucleus with a critical diameter  $x_c$  of 55 nm, undirected growth is possible until at least one dimension reaches 1.0  $\mu\text{m}$ , before the shear flow field orients the crystallite. As a result, the crystallite experiences directed growth at a later stage and the drag increase by growth into the y-axis is significantly reduced leading to crystallites of oblate rather than prolate shape. From the SEM images we cannot accurately determine the height (z-axis) of the imaged crystallites. The z-axis of the crystallites is expected to experience the strongest decrease with increasing  $\dot{\gamma}_{cryst}$  due to its lowest probability of growth into the shear gradient direction. To investigate the height profile of the formed crystallites, atomic force microscopy (AFM) was employed.

Fig. 6 shows the AFM (A-B) height and (C) amplitude image as well as (D-E) selected cross sections and (F) a histogram of the z-step size in a crystallite isolated from a TP-MCT CMS crystallized at  $\dot{\gamma}_{cryst} = 10^0 \text{ s}^{-1}$ . Figure S5 depicts additional height and amplitude images as well as cross sections of other crystallites produced at  $\dot{\gamma}_{cryst} = 10^0 \text{ s}^{-1}$ . Figs. 6(A,C) show an oblate crystallite with a height of 1  $\mu\text{m}$  and similar width and length of 3–4  $\mu\text{m}$  with 3 distinguishable domains based on the height information. Fig. 6(D) shows a domain height of 400–800 nm. Looking closer at a single

domain, discrete step sizes are measurable as shown in Fig. 6(B, E). Evaluating the step size of 69 z-steps, a z-step size histogram as shown in Fig. 6(F) is deduced. The mean step size is  $4.08 \pm 0.74 \text{ nm}$ .

Fig. 7 shows AFM (A-B) height and (C) amplitude image as well as (D-E) selected cross sections and (F) a histogram of the lamellar step size in a crystallite isolated from a TP-MCT CMS isothermally crystallized at  $\dot{\gamma}_{cryst} = 10^3 \text{ s}^{-1}$ . Figure S6 depicts additional height and amplitude images as well as cross sections of other crystallites produced at  $\dot{\gamma}_{cryst} = 10^3 \text{ s}^{-1}$ . Figs. 7(A,C) show a prolate crystallite with a height of 800 nm, a width of 1.0–2.0  $\mu\text{m}$ , and a length of 6  $\mu\text{m}$ . Figs. 7(A,C) allow to differentiate 3–4 domains based on the height information. Fig. 7(D) shows a domain height of 100–300 nm. Looking closer at a single domain, discrete step sizes are measurable as shown in Fig. 7(B,E). Evaluating the step size of 63 z-steps, a z-step size histogram as shown in Fig. 7(F) is depicted. The mean step size is  $4.3 \pm 0.84 \text{ nm}$ . The morphological information on the crystallites produced at  $\dot{\gamma}_{cryst} = 10^0$  and  $10^3 \text{ s}^{-1}$  teach that with increasing  $\dot{\gamma}_{cryst}$  the domain height and width decreases, while the domain length increases converting the oblate crystallites formed at  $\dot{\gamma}_{cryst} = 10^0 \text{ s}^{-1}$  to prolate crystallites at  $10^3 \text{ s}^{-1}$ . However, the total height of the crystallites is similar for  $\dot{\gamma}_{cryst} = 10^0$  and  $10^3 \text{ s}^{-1}$ , showing that the crosssectional crystallite area perpendicular to the flow direction is more important than absolute height. The acting shear flow field does not primarily affect overall crystallite height, but domain height, width, and length such that the overall crosssectional area perpendicular to the flow direction is

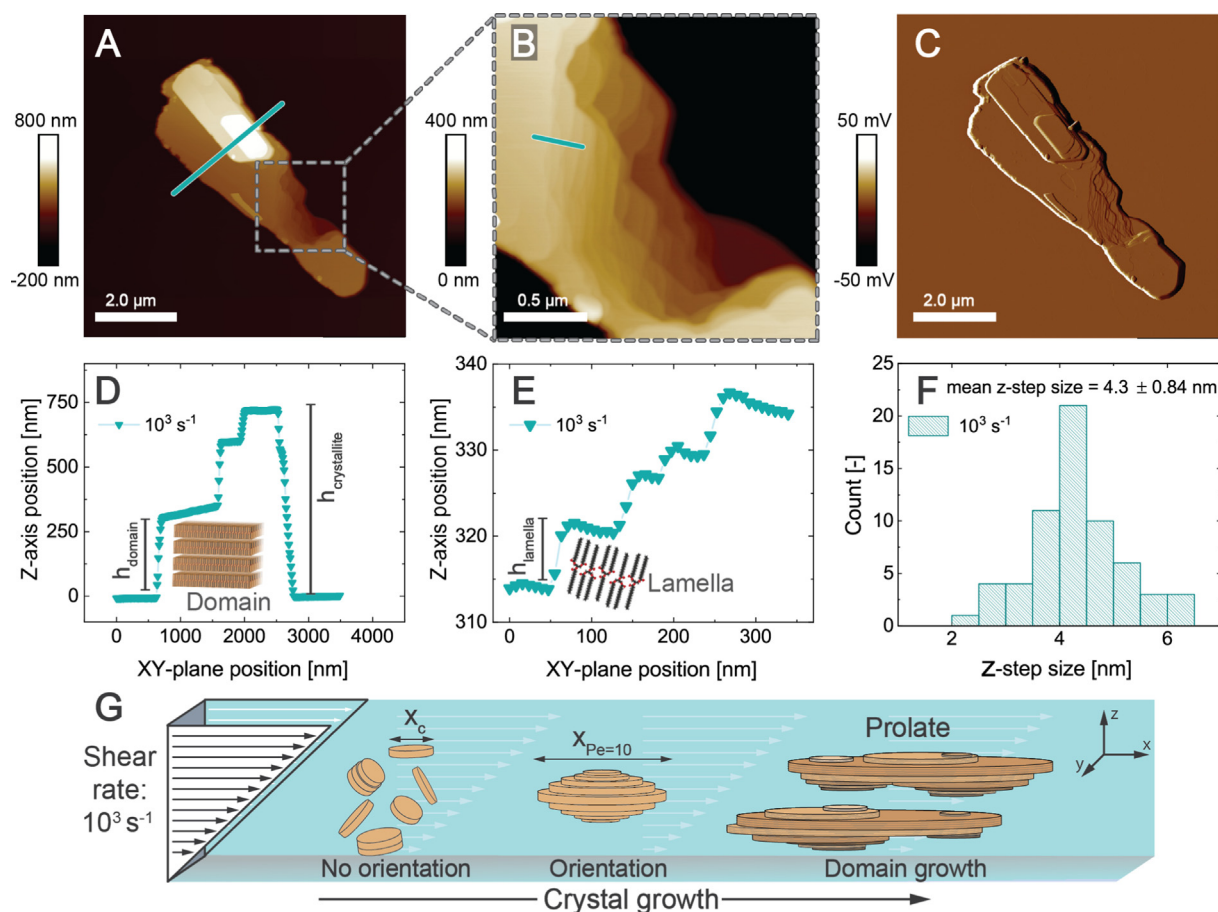


**Fig. 7.** AFM (A-B) height and (C) amplitude image of a crystallite isolated from TP-MCT CMS crystallized at  $\dot{\gamma}_{cryst} = 10^3 \text{ s}^{-1}$ . (D-E) are the z-axis readings as function of the xy-plane of the indicated turquoise lines in (A-B), respectively. (F) shows the histogram of the z-step size indicated in (E). A total of 63 steps were evaluated with a mean step size = 4.3 nm, a minimum step size = 2.40 nm, a maximum step size = 6.30 nm, and a median step size = 4.25 nm. (G) The proposed mechanism of nucleus growth and domain propagation into a crystallite at  $\dot{\gamma}_{cryst} = 10^3 \text{ s}^{-1}$ .



minimized. From the findings presented in Figs. 6(A,C,D) and 7(A,C,D) we suggest a mechanistic model of crystallite growth as displayed in Figs. 6(G) and 7(G): Firstly, the initial flat cylindrical nucleus with a critical diameter of  $x_c = 55$  nm and a height of approximately 4.5 nm is formed. The nucleus grows until one dimension reaches the critical length for orientation  $x_{pe10}$ . This dimension is streamlined parallel to the  $x$ -axis. Growth takes place mainly in the  $x$ -axis but also in the  $y$ -axis and eventually in the  $z$ -axis. The  $z$ -axis propagation is always less favorable compared to the  $y$ -axis propagation, since more additional drag is created. As soon as the length scale in the  $z$ -axis has reached  $x_{pe10}$ , a new domain will be formed. The new domain will have a reduced cross sectional area (reduced height and width) in the  $zy$ -plane, such that additionally created drag is minimized. The growth of the cross sectional area in the  $zy$ -plane creates a shear microgradient as observed in thrombus formation [41]. At the edges of the new domain, high shear rates act, whereas in the  $x$ -axis downstream direction of the domain low shear rates are prevalent. The slipstream creation of the new domain promotes propagation in the  $x$ -axis. Consequently, new domain formation depends highly on the  $\dot{\gamma}_{cryst}$  magnitude inducing overall crystallite drag reduction [43] and generation of shear micro gradients [41]. Not only does the shear flow field affect domain propagation, but also the TP acyl-chain length structure as illustrated in the  $z$ -step size profile and size histogram presented in Figs. 6(E,F) and 7(E,F). The mean  $z$ -step size of 4.08 and 4.30 nm corresponds to the lamellar thickness  $h_{lamella}$  judging from the previously reported  $\beta$ -TP  $d_{001}$  long spacing of 4.03–4.09 nm [21,22,27,10] and from the  $\beta$ -TP  $d_{001}$  XRD peaks shown in Figure S7. The measured  $h_{lamella}$  is higher compared to the  $d_{001}$  long spacing as a result of the triclinic crystal structure as illustrated in Figure S1. The difference between  $h_{lamella}$  and  $d_{001}$  is approximately one C-C bond length  $d_{C-C}$  amounting to approximately 0.15 nm [18] as illustrated in Figure S1. From the mean  $h_{lamella}$  the acyl-chain tilt angle  $\tau$  is calculated as:

$$\tau = 90 - \arccos \frac{h_{lamella}(\beta) - d_{C-C}(\beta)}{d_{001}(\alpha)} \quad (8)$$

where  $d_{001}(\alpha) = 4.56$  nm [10]. Solving Eq. 8 for  $\tau$  yields 59.5 and 65.5° for  $\beta$ -TP crystallized at  $\dot{\gamma}_{cryst} = 10^0$  s<sup>-1</sup> and  $\dot{\gamma}_{cryst} = 10^3$  s<sup>-1</sup>, respectively. The values of  $\tau$  are in good agreement with the values proposed by previous studies [31,13,19]. The histograms presented in Figs. 6(F) and 7(F) show that the lamellar thickness  $h_{lamella}$  and consequently  $\tau$  are not constant but distributed around a mean value. The distribution around the mean value depends on  $\dot{\gamma}_{cryst}$ : While Fig. 6(F) shows an asymmetric distribution with an abrupt decrease towards increased lamellar thicknesses as expected, Fig. 7(F) shows a symmetric  $z$ -step size distribution. The symmetric  $z$ -step size distribution points towards a modified DCL structure enabling a denser packing of the TAG molecules. The more densely packed DCL structure at high shear rates explains the increased peak melting temperature and broadened melting peak as well as the more prominent diffraction peak at  $2\theta = 19.8$  observed in Figure S4(A,D,E). Similar findings have been reported by Kellens et al. [21] for  $\beta$ -TP crystallized either indirectly from the  $\alpha$ -polymorph or directly from solvent and by Stuart et al. [55] for TP crystallized at  $10^1$  and  $10^3$  s<sup>-1</sup>. Solvent crystallization yielded higher melting  $\beta$ -TP which was ascribed to an improved three dimensional order of the crystal. From the findings presented in Fig. 6 and 7, the influence of shear flow field on the domain propagation and consequently on the acyl-chain length structure is elucidated. The domain propagation is governed by the overall drag reduction and the domain growth in the slipstream. Depending on  $\dot{\gamma}_{cryst}$ , the slow or rapid domain propagation leads to less or more densely packed DCL structures reflected by the diffraction and melting behavior of the  $\beta$ -TP crystallites.

## 5. Conclusion

The crystallization of lipids in laminar shear flows is a complex multiscale process which requires specific methods for each structural hierarchy level. We show how to characterize each structural level with the appropriate method for a model lipid composed of tripalmitin in MCT oil and derive a mechanistic understanding of the crystallization process. The impact of shear forces is quantified on all structural levels starting from the acyl-chain length structure to the aggregation of flocs into networks. At high crystallization shear rates  $\dot{\gamma}_{cryst}$ , the reduction of drag and the generation of micro gradients causing slipstreams are responsible for the formation of prolate crystallites with denser packed double chain length (DCL) structures. At low  $\dot{\gamma}_{cryst}$ , oblate crystallites with less densely packed DCL structures are formed. Irrespective of  $\dot{\gamma}_{cryst}$ , the crystallites aggregate into spherical clusters with similar diameters. The  $\dot{\gamma}_{cryst}$  determines the aggregation rate of the clusters into flocs and the equilibrium diameter of the flocs. At high  $\dot{\gamma}_{cryst}$ , clusters are formed rapidly and aggregate into small flocs forming weak networks. At low  $\dot{\gamma}_{cryst}$ , clusters form slowly and are therefore aggregating into large flocs which form strong networks.

Although further work is required to quantify nucleus growth and alignment *in situ*, our study offers both qualitative and quantitative ways to reconstruct the journey of a single TAG molecule crystallizing in laminar shear flow. We identified the morphology determining mechanism on each structural hierarchy level. This opens new possibilities to measure and control the structure formation of crystalline TAGs leading to the facilitated development of novel lipids with reduced SFA content but identical organoleptic properties compared to high SFA lipids contributing to a healthier and more sustainable diet.

## 6. Supporting Information

The following files are available free of charge.

- Schematic drawing of the double chain length (DCL) arrangement of triacylglycerols and the angle of tilt
- Additional PLM images of TP-MCT CMS crystallized at  $\dot{\gamma}_{cryst}$  of  $10^0$ ,  $10^1$ ,  $10^2$ , and  $10^3$  s<sup>-1</sup>
- The density distribution of TP-MCT CMS crystallized at  $\dot{\gamma}_{cryst} = 10^0$ ,  $10^1$ ,  $10^2$ , and  $10^3$  s<sup>-1</sup>
- XRD spectra and DSC thermograms of TP-MCT CMS crystallized at  $\dot{\gamma}_{cryst}$  of  $10^0$ ,  $10^1$ ,  $10^2$ , and  $10^3$  s<sup>-1</sup>
- Calculation regarding the critical nucleus diameter  $x_c$
- Additional AFM images and profiles for crystallites isolated from TP-MCT CMS crystallized at  $\dot{\gamma}_{cryst}$  of  $10^0$  and  $10^3$  s<sup>-1</sup>
- Small angle XRD of crystals isolated from TP-MCT CMS crystallized at  $\dot{\gamma}_{cryst}$  of  $10^0$  and  $10^3$  s<sup>-1</sup>

## 7. Author Contributions

Kim Mishra - conceptualization, project administration, investigation, methodology, supervision, software, validation, visualization, writing.

Nico Kummer - conceptualization, data curation, writing, investigation, methodology.

Jotam Bergfreund - data curation, data visualization.

Fabian Kämpf - data curation, formal analysis, investigation.

Pascal Bertsch - data curation, writing.

Robin Pauer - investigation, methodology.

Gustav Nyström - data curation, validation, funding acquisition.

Peter Fischer - data curation, validation, funding acquisition.

Erich J. Windhab - data curation, validation, funding acquisition.

## Declaration of Competing Interest

The authors declare that they have no known competing financial interests or personal relationships that could have appeared to influence the work reported in this paper.

## Acknowledgement

The authors express their gratefulness to the Swiss National Science Foundation and Innosuisse for funding of the Bridge project 20B2-1–180971/1.

## Appendix A. Supplementary material

Supplementary data associated with this article can be found, in the online version, at <https://doi.org/10.1016/j.jcis.2022.10.005>.

## References

- [1] N.C. Acevedo, A.G. Marangoni, Characterization of the nanoscale in triacylglycerol crystal networks, *Cryst. Growth Des.* 10 (2010) 3327–3333, <https://doi.org/10.1021/cg100468e>.
- [2] N.C. Acevedo, A.G. Marangoni, Toward nanoscale engineering of triacylglycerol crystal networks, *Cryst. Growth Des.* 10 (2010) 3334–3339.
- [3] M. Bayard, B. Kauffmann, J.-M. Vauvre, F. Leal-Calderon, M. Cansell, Isothermal crystallization of anhydrous milk fat in presence of free fatty acids and their esters: From nanostructure to textural properties, *Food Chem.* 366 (2022) 130533.
- [4] J. Bergfreund, P. Bertsch, S. Kuster, P. Fischer, Effect of oil hydrophobicity on the adsorption and rheology of  $\beta$ -lactoglobulin at oil–water interfaces, *Langmuir* 34 (2018) 4929–4936, <https://doi.org/10.1021/acs.langmuir.8b00458>. URL: <https://pubs.acs.org/doi/10.1021/acs.langmuir.8b00458>.
- [5] H. Bunjes, Structural properties of solid lipid based colloidal drug delivery systems, *Curr. Opin. Colloid Interface Sci.* 16 (2011) 405–411.
- [6] G. Calvert, A. Hassanpour, M. Ghadiri, Mechanistic analysis and computer simulation of the aerodynamic dispersion of loose aggregates, *Chem. Eng. Res. Des.* 89 (2011) 519–525.
- [7] K.M. Carlson, R. Heilmayr, H.K. Gibbs, P. Noojipady, D.N. Burns, D.C. Morton, N. F. Walker, G.D. Paoli, C. Kremen, Effect of oil palm sustainability certification on deforestation and fire in Indonesia, *Proc. Nat. Acad. Sci.* 115 (2018) 121–126.
- [8] A. Chajchir, I. Benzaquen, E. Wexler, A. Arellano, Fat injection, *Aesthetic plastic surgery* 14 (1990) 127–136.
- [9] J. Chen, S.M. Ghazani, J.A. Stobbs, A.G. Marangoni, Tempering of cocoa butter and chocolate using minor lipidic components, *Nature Communications* 12 (2021) 1–9.
- [10] C.E. Clarkson, T. Malkin, Alternation in long-chain compounds. part ii. an x-ray and thermal investigation of the triglycerides, *Journal of the Chemical Society (Resumed)* 139 (1934) 666–671.
- [11] J. Deman, A. Beers, Fat crystal networks: structure and rheological properties, *Journal of Texture Studies* 18 (1987) 303–318.
- [12] V.A. Fernandes, A.J. Müller, A.J. Sandoval, Thermal, structural and rheological characteristics of dark chocolate with different compositions, *J. Food Eng.* 116 (2013) 97–108.
- [13] E. Frede, D. Precht, Molekülanordnungen in fetten mit trikliner kristallstruktur, *Fette, Seifen, Anstrichmittel* 79 (1977) 69–75.
- [14] S.M. Ghazani, A.G. Marangoni, Microbial lipids for foods, *Trends in Food Science & Technology* (2021).
- [15] Ghosh, S., & Rousseau, D. (2011). Fat crystals and water-in-oil emulsion stability. *Current Opinion in Colloid & Interface Science*, 16, 421–431. URL: <https://linkinghub.elsevier.com/retrieve/pii/S1359029411000823>. doi:10.1016/j.cocis.2011.06.006.
- [16] A.J. Gravelle, A.G. Marangoni, Ethylcellulose oleogels: Structure, functionality, and food applications, *Advances in food and nutrition research* 84 (2018) 1–56.
- [17] I. Heertje, M. Leunis, Measurement of shape and size of fat crystals by electron microscopy, *LWT-Food Science and Technology* 30 (1997) 141–146.
- [18] L. Jensen, A. Mabis, Refinement of the structure of  $\beta$ -tricaprin, *Acta Crystallogr. A* 21 (1966) 770–781.
- [19] S. de Jong, T. Van Soest, Crystal structures and melting points of saturated triglycerides in the  $\beta$ -2 phase, *Acta Crystallographica Section B: Structural Crystallography and Crystal Chemistry* 34 (1978) 1570–1583.
- [20] K. Kafui, C. Thornton, Numerical simulations of impact breakage of a spherical crystalline agglomerate, *Powder Technol.* 109 (2000) 113–132.
- [21] Kellens, M., Meeussen, W., & Reynaers, H. (1990a). Crystallization and phase transition studies of tripalmitin. *Chemistry and Physics of Lipids*, 55, 163–178. URL: <https://linkinghub.elsevier.com/retrieve/pii/0009308490900775>. doi:10.1016/0009-3084(90)90077-5.
- [22] Kellens, M., Meeussen, W., Riekel, C., & Reynaers, H. (1990b). Time resolved x-ray diffraction studies of the polymorphic behaviour of tripalmitin using synchrotron radiation. *Chemistry and Physics of Lipids*, 52, 79–98. URL: <https://linkinghub.elsevier.com/retrieve/pii/0009308490901531>. doi:10.1016/0009-3084(90)90153-1.
- [23] R.G. Larson, *The structure and rheology of complex fluids*, Oxford University Press, New York, 1999.
- [24] Larsson, K., Cyvin, S.J., Rymo, L., Bowie, J.H., Williams, D.H., Bunnenberg, E., Djerassi, C., & Records, R. (1966). Classification of glyceride crystal forms. *Acta Chemica Scandinavica*, 20, 2255–2260. URL: <http://acta.chem.scand.org/doi/10.3891/acta.chem.scand.20-2255>. doi:10.3891/acta.chem.scand.20-2255.
- [25] B.J. Le Révérend, I.T. Norton, P.W. Cox, F. Spyropoulos, Colloidal aspects of eating, *Current Opinion in Colloid & Interface Science* 15 (2010) 84–89, <https://doi.org/10.1016/j.cocis.2009.11.009>.
- [26] H.N. Lida, K. Sundram, W. Siew, A. Aminah, S. Mamot, TAG composition and solid fat content of palm oil, sunflower oil, and palm kernel olein belends before and after chemical interesterification, *J. Am. Oil. Chem. Soc.* 79 (2002) 1137–1144.
- [27] E. Lutton, The polymorphism of tristearin and some of its homologs, *J. Am. Chem. Soc.* 67 (1945) 524–527.
- [28] E. Lutton, Triple chain-length structures of saturated triglycerides, *J. Am. Chem. Soc.* 70 (1948) 248–254.
- [29] A.G. Marangoni, N. Acevedo, F. Maleky, F. Peyronel, G. Mazzanti, B. Quinn, D. Pink, et al., Structure and functionality of edible fats, *Soft Matter* 8 (2012) 1275–1300.
- [30] A.G. Marangoni, J.P. Van Duynhoven, N.C. Acevedo, R.A. Nicholson, A.R. Patel, Advances in our understanding of the structure and functionality of edible fats and fat mimetics, *Soft Matter* 16 (2020) 289–306, <https://doi.org/10.1039/C9SM01704F>.
- [31] A.G. Marangoni, L.H. Wesdorp, Structure and properties of fat crystal networks, CRC Press, 2019.
- [32] K.J. Martens, G. van Dalen, P.C. Heussen, M.A. Voda, T. Nikolaeva, J.P. van Duynhoven, Quantitative structural analysis of fat crystal networks by means of raman confocal imaging, *J. Am. Oil. Chem. Soc.* 95 (2018) 259–265.
- [33] G. Mazzanti, S.E. Guthrie, E.B. Sirota, A.G. Marangoni, S.H. Idziak, Orientation and phase transitions of fat crystals under shear, *Crystal Growth & Design* 3 (2003) 721–725, <https://doi.org/10.1021/cg034048a>.
- [34] K. Mishra, J. Bergfreund, P. Bertsch, P. Fischer, E.J. Windhab, Crystallization-induced network formation of tri- and monopalmitin at the middle-chain triglyceride oil/air interface, *Langmuir* 36 (2020) 7566–7572, <https://doi.org/10.1021/acs.langmuir.0c01195>. URL: <https://pubs.acs.org/doi/10.1021/acs.langmuir.0c01195>.
- [35] Mishra, K., Dufour, D., & Windhab, E.J. (2020b). Yield stress dependent foaming of edible crystal-melt suspensions. *Crystal Growth & Design*, 20, 1292–1301. URL: <https://pubs.acs.org/doi/abs/10.1021/acs.cgd.9b01558> <https://pubs.acs.org/doi/10.1021/acs.cgd.9b01558>. doi:10.1021/acs.cgd.9b01558.
- [36] K. Mishra, L. Grob, L. Kohler, S. Zimmermann, S. Gstöhl, P. Fischer, E.J. Windhab, Entrance flow of unfoamed and foamed herschel-bulkley fluids, *J. Rheol.* 65 (2021) 1155–1168, <https://doi.org/10.1122/8.0000286>.
- [37] K. Mishra, L. Kohler, N. Kummer, S. Zimmermann, S. Ehrenguber, F. Kämpf, D. Dufour, G. Nyström, P. Fischer, E.J. Windhab, Rheology of cocoa butter, *J. Food Eng.* 305 (2021) 110598, <https://doi.org/10.1016/j.jfoodeng.2021.110598>.
- [38] K.S. Mishra, F. Kämpf, S. Ehrenguber, J. Merkel, N. Kummer, R. Pauer, P. Fischer, E. Windhab, The rheology and foamability of crystal-melt suspensions composed of triacylglycerols, *Soft Matter* (2022).
- [39] M. Motoyama, K. Chikuni, T. Narita, K. Aikawa, K. Sasaki, In situ raman spectrometric analysis of crystallinity and crystal polymorphism of fat in porcine adipose tissue, *J. Agric. Food. Chem.* 61 (2013) 69–75.
- [40] S.S. Narine, A.G. Marangoni, Relating structure of fat crystal networks to mechanical properties: a review, *Food Res. Int.* 32 (1999) 227–248.
- [41] W.S. Nesbitt, E. Westein, F.J. Tovar-Lopez, E. Tolouei, A. Mitchell, J. Fu, J. Carberry, A. Fouras, S.P. Jackson, A shear gradient-dependent platelet aggregation mechanism drives thrombus formation, *Nat. Med.* 15 (2009) 665–673.
- [42] R.A. Nicholson, A.G. Marangoni, Enzymatic glycerolysis converts vegetable oils into structural fats with the potential to replace palm oil in food products, *Nature Food* 1 (2020) 684–692.
- [43] D. Njobuenwu, M. Fairweather, Effect of shape on inertial particle dynamics in a channel flow, *Flow, Turbulence and Combustion* 92 (2014) 83–101.
- [44] F. Peyronel, J. Ilavsky, G. Mazzanti, A.G. Marangoni, D.A. Pink, Edible oil structures at low and intermediate concentrations. ii. ultra-small angle x-ray scattering of in situ tristearin solids in triolein, *J. Appl. Phys.* 114 (2013) 234902.
- [45] D.A. Pink, F. Peyronel, B. Quinn, P. Singh, A.G. Marangoni, Condensation versus diffusion. a spatial-scale-independent theory of aggregate structures in edible oils: applications to model systems and commercial shortenings studied via rheology and usaxs, *J. Phys. D: Appl. Phys.* 48 (2015) 384003.
- [46] D.A. Pink, B. Quinn, F. Peyronel, A.G. Marangoni, Edible oil structures at low and intermediate concentrations. i. modeling, computer simulation, and predictions for x ray scattering, *J. Appl. Phys.* 114 (2013) 234901.
- [47] A. Pizzirusso, F. Peyronel, E.D. Co, A.G. Marangoni, G. Milano, Molecular insights into the eutectic tripalmitin/tristearin binary system, *J. Am. Chem. Soc.* 140 (2018) 12405–12414.
- [48] D. Quemada, Rheological modelling of complex fluids. i. the concept of effective volume fraction revisited. *The European Physical Journal-Applied, Physics* 1 (1998) 119–127, <https://doi.org/10.1021/cg100468e>.
- [49] B. Quinn, F. Peyronel, T. Gordon, A. Marangoni, C.B. Hanna, D.A. Pink, Aggregation in complex triacylglycerol oils: coarse-grained models,

- nanophase separation, and predicted x-ray intensities, *J. Phys.: Condens. Matter* 26 (2014) 464108.
- [50] D. Rousseau, Fat crystals and emulsion stability—a review, *Food Res. Int.* 33 (2000) 3–14.
- [51] A.Y. Sajjadi, D. Manstein, S.A. Carp, Measuring temperature induced phase change kinetics in subcutaneous adipose tissues using near infrared spectroscopy, mr imaging and spectroscopy and oct, *Scientific Reports* 7 (2017) 17786.
- [52] K. Sato, Crystallization behaviour of fats and lipids — a review, *Chem. Eng. Sci.* 56 (2001) 2255–2265, [https://doi.org/10.1016/S0009-2509\(00\)00458-9](https://doi.org/10.1016/S0009-2509(00)00458-9).
- [53] Sato, K., & Ueno, S. (2011). Crystallization, transformation and microstructures of polymorphic fats in colloidal dispersion states. *Current Opinion in Colloid & Interface Science*, 16, 384–390. URL: <https://linkinghub.elsevier.com/retrieve/pii/S135902941100080X>. doi:10.1016/j.cocis.2011.06.004.
- [54] N. Siraj, M.A. Shabbir, T. Ahmad, A. Sajjad, M.R. Khan, M.I. Khan, M.S. Butt, Organogelators as a saturated fat replacer for structuring edible oils, *Int. J. Food Prop.* 18 (2015) 1973–1989.
- [55] B. Stuart, H. Maynard-Casely, N. Booth, A. Leung, P. Thomas, Neutron diffraction of deuterated tripalmitin and the influence of shear on its crystallisation, *Chem. Phys. Lipids* 221 (2019) 108–113.
- [56] Svanberg, L., Ahm  , L., Lor  n, N., & Windhab, E. (2013). Impact of pre-crystallization process on structure and product properties in dark chocolate. *Journal of Food Engineering*, 114, 90–98. URL: <https://linkinghub.elsevier.com/retrieve/pii/S0260877412003123>. doi:10.1016/j.jfoodeng.2012.06.016.
- [57] D. Tang, A.G. Marangoni, Quantitative study on the microstructure of colloidal fat crystal networks and fractal dimensions, *Adv. Colloid Interface Sci.* 128 (2006) 257–265, <https://doi.org/10.1016/j.cis.2006.11.019>.
- [58] V. Vijay, S.L. Pimm, C.N. Jenkins, S.J. Smith, The impacts of oil palm on recent deforestation and biodiversity loss, *PloS One* 11 (2016) e0159668.
- [59] E. Windhab, Untersuchungen zum rheologischen Verhalten konzentrierter Suspensionen, volume 3, VDI-Verlag, 1986.
- [60] E. Windhab, A new method for describing the time-dependent rheological behaviour of concentrated suspensions, in: *In Progress and Trends in Rheology II*, Steinkopff, Heidelberg, 1988, pp. 317–320, [https://doi.org/10.1007/978-3-642-49337-9\\_108](https://doi.org/10.1007/978-3-642-49337-9_108). URL: [http://link.springer.com/10.1007/978-3-642-49337-9\\_108](http://link.springer.com/10.1007/978-3-642-49337-9_108).
- [61] E.J. Windhab, Fluid immobilization—a structure-related key mechanism for the viscous flow behavior of concentrated suspension systems, *Applied Rheology* 10 (2000) 134–144.
- [62] A.N. Zdravkova, J. Van der Eerden, Structure and stability of triglyceride monolayers on water and mica surfaces, *Cryst. Growth Des.* 7 (2007) 2778–2787.